Supporting Information for "Autonomous biogeochemical floats detect significant carbon dioxide outgassing in the high-latitude Southern Ocean"

Alison R. Gray[1], Kenneth S. Johnson[2], Seth M. Bushinsky[3], Stephen C. Riser[1], Joellen L. Russell[4], Lynne D. Talley[5], Rik Wanninkhof[6], Nancy L. Williams[7], and Jorge L. Sarmiento[3]

[1]School of Oceanography, University of Washington, Seattle, Washington 98195, USA.

[2]Monterey Bay Aquarium Research Institute, Moss Landing, California 95039, USA.

[3]Program in Atmospheric and Oceanic Sciences, Princeton University, Princeton, New Jersey 08544, USA.

[4]Department of Geosciences, University of Arizona, Tucson, Arizona 85721, USA.

[5]Scripps Institution of Oceanography, University of California San Diego, La Jolla, California 92093, USA.

[6]Atlantic Oceanographic and Meteorological Laboratory, National Oceanic and Atmospheric Administration, Miami, Florida 33149, USA.

[7]College of Earth, Ocean, and Atmospheric Sciences, Oregon State University, Corvallis, Oregon 97331 USA.

Contents of this file

3. Tables S1 to S2

Text S1. Biogeochemical Profiling Float Data This study used data from 35 of the 45 autonomous profiling floats built at the University of Washington and deployed by the SOCCOM program prior to July 2016 (float information given in Table S1). The remaining floats were excluded because they lacked a pH sensor (6) or the pH sensor failed within one month of deployment (4). Fifteen floats were deployed in the Pacific sector of the Southern Ocean from three separate research cruises (Sloyan & Wijffels, 2016; Talley, Johnson, Riser, & Hennon, 2014; Weller, 2015), eleven were deployed in the Atlantic sector from two cruises (Boebel, 2015; Firing, 2016), and the remaining nine were deployed in the Indian sector from four cruises (Cofin, 2016; MacDonald, 2016; Trull, 2015, 2016). All deployments were accompanied by high-accuracy shipboard data collection to provide an independent quality assessment and validation of the float sensors. Each float executed a mission cycle (over either 5 or 10 days) that consisted of an initial descent to about 1000 m, drift with the predominant currents at that depth for a specified period of time (approximately 4 or 9 days), descent to about 2000 m followed by a profile from that depth to the surface. Once at the surface, each float transmitted its data via telecommunication satellites to a shore-based data center and obtained a fix of its location via GPS.

On each float, a conductivity-temperature-depth sensor (SeaBird Model 41CP) reported bin-averaged S, T, and p at 2-m vertical resolution above 1000 m and 100-m vertical resolution below. In addition, each float was equipped with sensors to measure chemical properties of the water at variable vertical resolution (approximately 5 m above 100 m depth and gradually increasing to 100 m below 1000 m). An optode (Aanderaa 4330) (Tengberg

et al., 2006) measured the concentration of dissolved O_2 on every float. Observations of atmospheric O_2 values were collected at the surface to enable accurate calibration of the sensor data (Johnson, Plant, Riser, & Gilbert, 2015), which were also compared with the shipboard bottle O_2 data. Thirty-three of the 35 floats had an ultraviolet spectrophotometer (ISUS) (Johnson et al., 2013) that measured NO_3 concentration. Four of these failed shortly after deployment, leaving 29 floats with working NO_3 sensors. The float NO_3 data were adjusted using a multiple linear regression at 1500 m depth (Williams et al., 2016), and the adjusted data were validated by comparing to shipboard bottle NO_3 samples measured on the deployment cruises (Johnson et al., 2017). On every float, pH was measured by an ion-sensitive field effect transistor (Deep-Sea DuraFET) (Johnson et al., 2016) and reported on the total hydrogen ion scale at in situ T and p. The data were corrected for sensor drift in near real-time by performing minimal adjustments of the sensor calibration to align pH measured at 1500 m with pH estimated from measured T, S, p and O_2 using an empirical multiple linear regression algorithm trained with high-quality bottle pH data collected during recent Southern Ocean cruises (Wanninkhof et al., 2016; Williams et al., 2016). After this adjustment, the final pH values were consistent with independent shipboard measurements, with the standard deviation of the differences equal to 0.007 (Johnson et al., 2016).

Text S2. Float-based Estimates of Air-Sea CO_2 Flux Air-sea CO_2 flux F was calculated along each float path from (Wanninkhof, 2014)

$$F = k\,K_0\,(p\mathrm{CO}_2^{\mathrm{ocn}} - p\mathrm{CO}_2^{\mathrm{atm}}), \tag{1}$$

where k is the gas transfer velocity, K_0 is the solubility, pCO_2^{ocn} and pCO_2^{atm} are the partial pressures of CO_2 in the ocean and atmosphere, respectively.

Measured pH was combined with an empirical estimate of total alkalinity A_T to calculate the remaining parameters in the carbon system, total carbon C_T and pCO_2^{ocn} at in situ T and S, using the dissociation constants of fluoride from Perez and Fraga (1987); of sulfate from Dickson (1990); of carbonate from Lueker, Dickson, and Keeling (2000); and the boron to salinity ratio of Lee et al. (2010). A number of different empirical methods have been proposed to estimate A_T from measured seawater properties; two different algorithms were tested here in order to gauge the sensitivity of the results to A_T. The choice of alkalinity estimation method is not expected to have a strong impact, as when A_T and pH are used together to calculate pCO_2, the resulting pCO_2 depends very strongly on pH and changes in A_T have little influence (Williams et al., 2017). Both the locally-interpolated alkalinity regression (LIARv2; Carter et al., 2018) and the Southern Ocean-specific multiple linear regression (Williams et al., 2017) calculate A_T as a function of T, S, p, and O_2, but they are based on differing sets of high-quality shipboard A_T measurements. The mean difference between the resulting A_T estimates was found to be 5.5 ± 6.4 µmol kg^{-1}, which lies within the given uncertainty estimates for both methods and results in a mean pCO_2^{ocn} difference of 1.0 ± 1.2 µatm. Differences of less than 0.03 PgC y^{-1} were found in the estimates of annual net CO_2 uptake in each region when using these two algorithms to compute A_T. The results shown here use the A_T estimate calculated with the LIARv2 method. Furthermore, a bias arises when calculating pCO_2^{ocn} from pH and A_T, due to uncertainties in both the equilibrium constants and the shipboard pH data

used in calibration (see Williams et al. (2017) for detailed explanation and characterization of bias). The pCO_2^{ocn} values calculated here were corrected for this bias, which varies with pH, using the empirical relationship developed by Williams et al. (2017). A recent assessment using a much larger set of ship-board data found a very similar relationship (Carter et al., 2018).

To test the sensitivity of the results to the depth sampling scheme, the seawater properties used in the flux calculation (T, S, and pCO_2^{ocn}) were determined in three different ways: 1) the value at the uppermost pressure at each profile, typically 5-7 m, 2) an average of in situ values over the mixed layer (with the mixed layer depth defined as the depth where the density was 0.03 kg m^{-3} greater than the uppermost density (de Boyer Montégut, Madec, Fischer, Lazar, & Iudicone, 2004)), and 3) an average of in situ values over the upper 20 m or the mixed layer if it was shallower than 20 m. The results were negligibly different except when the mixed layer exceeded about 400 m, and the associated changes in the annual net flux estimates for each region were less than 0.04 PgC y^{-1}. The fluxes given here use surface ocean properties calculated as the average over the upper 20 m.

A squared wind speed-dependent parameterization (Wanninkhof, 2014) was used to compute k in (1) from the Schmidt number (calculated with the float-measured T and S) together with an estimate of the 10-m wind speed (U_{10}). To assess the sensitivity to the choice of wind product, k was computed using 6-hourly wind speeds at 0.75° horizontal resolution from the ERA-Interim Reanalysis (Dee et al., 2011) provided by the European Centre for Medium-Range Weather Forecasting (ECMWF) and daily-averaged wind

speeds at 0.25° horizontal resolution based on observations from the Metop/ASCAT satellite (Bentamya & Fillona, 2012), obtained from the Centre de Recherche et d'Exploitation Satellitaire (CERSAT) at IFREMER, Plouzané (France). For each wind product, the float trajectories, measured T and S, and float-based $p\mathrm{CO_2}^{\mathrm{ocn}}$ were interpolated between consecutive profiles using piecewise cubic Hermite polynomials, to the times of the wind speed estimates. The gridded wind fields were then interpolated spatially to the location of the float and used with T and S to compute k at either 6-hour or daily intervals. Solubility K_0 was calculated at the same frequency from the interpolated T and S using the fit provided by Weiss (1974).

To estimate $p\mathrm{CO_2}^{\mathrm{atm}}$, observations of the mole fraction of $\mathrm{CO_2}$ in dry air were taken from monthly measurements of air samples at the Cape Grim Observatory in Tasmania, Australia and interpolated using piecewise cubic Hermite polynomials to the times of the wind speed estimates. These values were then combined with an estimate of the mean sea level pressure (SLP) at the float location, corrected for water vapor pressure using the method of Zeebe and Wolf-Gladrow (2001), to give $p\mathrm{CO_2}^{\mathrm{atm}}$ at the float position. When ERA-Interim winds were used, SLP was obtained from the same product; when satellite ASCAT winds were used, SLP was taken from NCEP Reanalysis 6-hourly fields (Kalnay et al., 1996). For each float profile, SLP was averaged over the preceding month to account for the equilibrium time of air-sea gas exchange of $\mathrm{CO_2}$, although results were unchanged when instantaneous SLP was used.

The flux F was calculated from these quantities according to equation (1). Sea ice concentration C_{SI} along each float trajectory was determined from daily satellite observa-

tions of sea ice extent (Cavalieri, Parkinson, Gloersen, & Zwally, 1996). For the estimates made using ERA-Interim winds, the air-sea flux at each time was adjusted by a factor of $(1-C_{SI})$ to account for the reduction in flux due to sea ice cover. All values of $C_{SI} > 95\%$ were set equal to 95% to account for sea ice leads following the methods of Takahashi et al. (2009). The ASCAT satellite is unable to retrieve a wind speed in the presence of sea ice; for these estimates the flux was assumed to be zero when sea ice was detected. The differences in annual net uptake obtained using the two wind products were less than 0.01 PgC y^{-1} for all zones except the seasonally ice-covered region, where the change rose to 0.03 PgC y^{-1}. The values shown here are those derived using the ERA-Interim fields.

Text S3. Definition of Southern Ocean Zones The Southern Ocean south of 35°S was divided into five different zones by applying the criteria of Orsi, Whitworth, and Nowlin (1995) to a mean 2014-2016 Argo-based climatology of temperature and salinity (Roemmich & Gilson, 2009). The STZ was defined as the region north of the Subtropical Front (STF), taken as the location where potential temperature (θ) at 100 m is equal to 11°C. The SAZ was designated as the region between the STF and the Subantarctic Front (SAF), defined as the location where θ at 400 m is equal to 5°C. The PFZ was defined as the region bounded by the SAF on the north and the Polar Front (PF) on the south. The PF was determined as the location where θ equals 2°C along the θ-minimum in the upper 200 m. Further to the south, the Antarctic-Southern Zone encompassed the area between the PF on the north and the mean 2014-2016 September sea ice extent (defined as the location with 15% sea ice concentration), as determined by Nimbus satellite sea ice observations (Cavalieri et al., 1996). The SIZ was defined as the region south of that

boundary not covered by ice sheets. The area of each region (Table SS2) was determined, excluding all 1° grid boxes with mean bottom depths less than 1000 m.

Text S4. Uncertainty Estimates for Float-based Fluxes The total uncertainty in the air-sea flux F for each float was derived from uncertainties in each of the terms in equation (1) using a Monte Carlo simulation of the full calculation, with 5000 iterations. To estimate the uncertainty introduced by spatio-temporal variability in each zone, the standard error was computed from the variance in the monthly mean flux estimates in each zone, taking into account the auto-correlation in the seasonal cycle of flux. These two uncertainty estimates were then added in quadrature to give the total uncertainty in the annual net flux in each region.

The total uncertainty in float-based $p\mathrm{CO_2}^{\mathrm{ocn}}$ results from uncertainties in the pH, estimated A_T, and equilibrium constants used to calculate $p\mathrm{CO_2}$. Propagating all of these sources of uncertainty in a top-down approach gives a predicted error in $p\mathrm{CO_2}^{\mathrm{ocn}}$ with a standard deviation of 2.86% (11.4 µatm at a $p\mathrm{CO_2}^{\mathrm{ocn}}$ of 400 µatm). This value is based on an update to the analysis of Williams et al. (2017) to reflect an increased uncertainty in the O_2 data used to adjust the pH sensor (from ±0.4% to ±1%). In the Monte Carlo simulation, this total uncertainty in $p\mathrm{CO_2}^{\mathrm{ocn}}$ was divided into two parts to reflect the understanding of the various sources of uncertainty (Williams et al., 2017). The first component, normally distributed with a standard deviation of 2.2%, was applied randomly to each float-based estimate of $p\mathrm{CO_2}^{\mathrm{ocn}}$; the second component, normally distributed with a standard deviation of 1.8%, was applied systematically to all floats (i.e., as an offset to all float-based $p\mathrm{CO_2}^{\mathrm{ocn}}$ values).

The uncertainties in T and S were taken to be uniformly distributed within the range $\pm$ 0.002°C and $\pm$ 0.01, respectively. The uncertainty in k was estimated from the uncertainties in the measured T and S, the uncertainty in U_{10}, and other uncertainties in the model as described by Wanninkhof (2014) that amount to 12.5% plus an additional 10% when $U_{10} < 3.5$ m s^{-1}. Since no uncertainty estimate was provided for the reanalysis wind product, a normally-distributed error with a standard deviation of 1.5 m s^{-1} was assumed based on a comparison with satellite-derived observations (Chaudhuri, Ponte, Forget, & Heimbach, 2013). The uncertainty in K_0 was calculated from the uncertainty in T and S. The uncertainty in $pCO_2{}^{atm}$ was determined from the provided standard deviation for the observed values of the mole fraction of CO_2. A potential bias in SLP of $\pm$1 hPa was assumed for the entire region based on a comparison with in situ data (Salstein, Ponte, & Cady-Pereira, 2008). The uncertainty in $pCO_2{}^{atm}$ was considered to be spatially correlated among all floats.

References

Bentamya, A., & Fillona, D. C. (2012). Gridded surface wind fields from Metop/ASCAT measurements. *Int. J. Remote Sens.*, *33*(6), 1729-1754. doi: 10.1080/01431161.2011.600348

Boebel, O. (2015). *The Expedition PS89 of the Research Vessel POLARSTERN to the Weddell Sea in 2014/2015* (Tech. Rep.). Alfred Wegener Institute Report 689, http://doi.org/10.2312/BzPM_0689_2015.

Carter, B. R., Feely, R. A., Williams, N. L., Dickson, A. G., Fong, M. B., & Takeshita, Y. (2018). Updated methods for global locally interpolated estimation of alkalinity, pH,

and nitrate. *Limnol. Oceanogr.-Meth.*, *16*(2), 119-131. doi: 10.1002/lom3.10232

Cavalieri, D. J., Parkinson, C. L., Gloersen, P., & Zwally, H. J. (1996). *Sea Ice Concentrations from Nimbus-7 SMMR and DMSP SSM/I-SSMIS Passive Microwave Data, Version 1.* (Tech. Rep.). NASA National Snow and Ice Data Center Distributed Active Archive Center doi:10.5067/8GQ8LZQVL0VL, accessed 01/09/2016.

Chaudhuri, A. H., Ponte, R. M., Forget, G., & Heimbach, P. (2013). A comparison of atmospheric reanalysis surface products over the ocean and implications for uncertainties in air-sea boundary forcing. *J. Climate*, *26*(1), 153-170. doi: 10.1175/JCLI-D-12-00090.1

Cofin, M. F. (2016). *RV Investigator Voyage Summary, Voyage IN2016_v01* (Tech. Rep.). Commonwealth Scientific and Industrial Research Organisation, https://soccom.princeton.edu/sites/default/files/media/pdf/IN2016_V01_Voyage_Summary_20160616.pd

de Boyer Montégut, C., Madec, G., Fischer, A. S., Lazar, A., & Iudicone, D. (2004). Mixed layer depth over the global ocean: An examination of profile data and a profile-based climatology. *J. Geophys. Res. Oceans*, *109*(12). doi: 10.1029/2004JC002378

Dee, D. P., Uppala, S. M., Simmons, A. J., Berrisford, P., Poli, P., Kobayashi, S., ... Vitart, F. (2011). The ERA-Interim reanalysis: Configuration and performance of the data assimilation system. *Q. J. Roy. Meteor. Soc.*, *137*(656), 553-597. doi: 10.1002/qj.828

Dickson, A. G. (1990). Thermodynamics of the dissociation of boric acid in synthetic seawater from 273.15 to 318.15 K. *Deep-Sea Res.*, *37*(5), 755-766. doi: 10.1016/

0198-0149(90)90004-F

Firing, Y. (2016). *RRS James Clark Ross Cruise JR15003* (Tech. Rep.). National Oceanography Centre, Cruise Report No. 38, https://cchdo.ucsd.edu/data/12275/NOC_CR_38.pdf.

Garcia, H. E., Locarnini, R. A., Boyer, T. P., Antonov, J. I., Baranova, O., Zweng, M., ... Johnson, D. (2014). *World Ocean Atlas 2013, Volume 4: Dissolved Inorganic Nutrients (phosphate, nitrate, silicate)* (Tech. Rep.). NOAA Atlas NESDIS 76.

Johnson, K. S., Coletti, L. J., Jannasch, H. W., Sakamoto, C. M., Swift, D. D., & Riser, S. C. (2013). Long-term nitrate measurements in the ocean using the in situ ultraviolet spectrophotometer: Sensor integration into the APEX profiling float. *J. Atmos. Ocean. Tech.*, *30*(8), 1854-1866. doi: 10.1175/JTECH-D-12-00221.1

Johnson, K. S., Jannasch, H. W., Coletti, L. J., Elrod, V. A., Martz, T. R., Takeshita, Y., ... Connery, J. G. (2016). Deep-Sea DuraFET: A pressure tolerant pH sensor designed for global sensor networks. *Anal. Chem.*, *88*, 3429-3256. doi: 10.1021/acs.analchem.5b04653

Johnson, K. S., Plant, J. N., Coletti, L. J., Jannasch, H. W., Sakamoto, C. M., Riser, S. C., ... Sarmiento, J. L. (2017). Biogeochemical sensor performance in the SOCCOM profiling float array. *J. Geophys. Res.: Oceans*, *122*. doi: 10.1002/2017JC012838

Johnson, K. S., Plant, J. N., Riser, S. C., & Gilbert, D. (2015). Air oxygen calibration of oxygen optodes on a profiling float array. *J. Atmos. Ocean. Tech.*, *32*(11), 2160-2172. doi: 10.1175/JTECH-D-15-0101.1

Kalnay, E., Kanamitsu, M., Kistler, R., Collins, W., Deaven, D., Gandin, L., ... Joseph, D. (1996). The NCEP/NCAR 40-Year reanalysis project. *B. Am. Meteorol. Soc.*, *77*(3), 437-471. doi: 10.1175/1520-0477(1996)077⟨0437:TNYRP⟩2.0.CO;2

Le Quéré, C., Andrew, R. M., Friedlingstein, P., Sitch, S., Pongratz, J., Manning, A. C., ... Zhu, D. (2018). Global Carbon Budget 2017. *Earth Syst. Sci. Data*, *10*(1), 405–448. doi: 10.5194/essd-10-405-2018

Lee, K., Kim, T.-W., Byrne, R. H., Millero, F. J., Feely, R. A., & Liu, Y.-M. (2010). The universal ratio of boron to chlorinity for the North Pacific and North Atlantic oceans. *Geochim. Cosmochim. Ac.*, *74*(6), 1801-1811. doi: 10.1016/j.gca.2009.12.027

Lueker, T. J., Dickson, A. G., & Keeling, C. D. (2000). Ocean pCO_2 calculated from dissolved inorganic carbon, alkalinity, and equations for K_1 and K_2: Validation based on laboratory measurements of CO_2 in gas and seawater at equilibrium. *Mar. Chem.*, *70*(1), 105-119. doi: 10.1016/S0304-4203(00)00022-0

MacDonald, A. (2016). *Cruise Report of the 2016 I08S US GO-SHIP Reoccupation* (Tech. Rep.). U.S. GO-SHIP, https://cchdo.ucsd.edu/data/12419/33RR20160208_do.pdf.

Orsi, A. H., Whitworth, T., & Nowlin, W. D. (1995). On the meridional extent and fronts of the Antarctic Circumpolar Current. *Deep-Sea Res. Pt. I*, *42*(5), 641-673. doi: 10.1016/0967-0637(95)00021-W

Perez, F. F., & Fraga, F. (1987, jul). Association constant of fluoride and hydrogen ions in seawater. *Mar. Chem.*, *21*(2), 161-168. doi: 10.1016/0304-4203(87)90036-3

Roemmich, D., & Gilson, J. (2009). The 2004-2008 mean and annual cycle of temperature, salinity, and steric height in the global ocean from the Argo Program. *Prog.*

Oceanogr., *82*, 81-100. doi: 10.1016/j.pocean.2009.03.004

Salstein, D. A., Ponte, R. M., & Cady-Pereira, K. (2008). Uncertainties in atmospheric surface pressure fields from global analyses. *J. Geophys. Res.*, *113*, D14107. doi: 10.1029/2007JD009531

Sloyan, B., & Wijffels, S. (2016). *RV Investigator Voyage Summary, Voyage IN2016_v03* (Tech. Rep.). Commonwealth Scientific and Industrial Research Organisation, https://cchdo.ucsd.edu/data/12704/096U20160426_do.pdf.

Takahashi, T., Sutherland, S. C., Wanninkhof, R., Sweeney, C., Feely, R. A., Chipman, D. W., ... de Baar, H. J. W. (2009). Climatological mean and decadal change in surface ocean pCO_2 and net sea-air CO_2 flux over the global oceans. *Deep-Sea Res. Pt. II*, *56*(8-10), 554-577. doi: 10.1016/j.dsr2.2008.12.009

Talley, L. D., Johnson, K. S., Riser, S. C., & Hennon, T. C. (2014). *SOCCOM biogeochemical profiling float deployments from GO-SHIP P16S (RVIB Nathaniel B. Palmer NBP1403)* (Tech. Rep.). SOCCOM Tech. Rep. 2014-1, http://soccom.princeton.edu/sites/default/files/files/SOCCOM_2014-1_P16S_floats.pdf.

Tengberg, A., Hovdenes, J., Andersson, H. J., Brocandel, O., Diaz, R., Hebert, D., ... Stangelmayer, A. (2006). Evaluation of a lifetime-based optode to measure oxygen in aquatic systems. *Limnol. Oceanogr.-Meth.*, *4*, 7-17. doi: 10.4319/lom.2006.4.7

Trull, T. (2015). *RV Investigator Voyage Summary, Voyage IN2015_v01* (Tech. Rep.). Commonwealth Scientific and Industrial Research Organisation, http://soccom.princeton.edu/sites/default/files/files/IN2015_v01_Voyage_Summary_Chief_Scientist.pdf.

Trull, T. (2016). *RV Investigator Voyage Summary, Voyage IN2016_v02* (Tech. Rep.). Commonwealth Scientific and Industrial Research Organisation, https://soccom.princeton.edu/sites/default/files/files/IN2016_V02_VoyagePlan_SubmissiontoMNF_11Dec

Wanninkhof, R. (2014). Relationship between wind speed and gas exchange over the ocean revisited. *Limnol. Oceanogr.-Meth.*, *12*, 351-361. doi: 10.4319/lom.2014.12.351

Wanninkhof, R., Johnson, K., Williams, N., Sarmiento, J., Riser, S., Briggs, E., ... Verdy, A. (2016). *An evaluation of pH and NO_3 sensor data from SOCCOM floats and their utilization to develop ocean inorganic carbon products* (Tech. Rep.). SOCCOM Carbon System Working Group, http://soccom.princeton.edu/sites/default/files/files/CWG_white_paper_March_13_2016.pdf.

Weiss, R. (1974). Carbon dioxide in water and seawater: The solubility of a non-ideal gas. *Mar. Chem.*, *2*(3), 203-215. doi: 10.1016/0304-4203(74)90015-2

Weller, R. (2015). *Global Southern Ocean 1 Deployment* (Tech. Rep.). Ocean Observatories Initiative, No. 3201-00102, https://alfresco.oceanobservatories.org/alfresco/d/d/workspace/SpacesStore/c5d98550-f51a-47d2-be05-d45165c73835/3201-00102_Quick_Look_Report_Southern_Ocean_1_2015-05-26_Ver_1-00.pdf.

Williams, N. L., Juranek, L. W., Feely, R. A., Johnson, K. S., Sarmiento, J. L., Talley,

L. D., ... Riser, S. C. (2017). Calculating surface ocean pCO_2 from biogeochemical Argo floats equipped with pH: An uncertainty analysis. *Global Biogeochem. Cycles*, *31*, 591–604. doi: 10.1002/2016GB005541

Williams, N. L., Juranek, L. W., Johnson, K. S., Feely, R. A., Riser, S. C., Talley, L. D., ... Wanninkhof, R. (2016). Empirical algorithms to estimate water column pH in the Southern Ocean. *Geophys. Res. Lett.*, *43*(7), 3415-3422. doi: 10.1002/2016GL068539

Zeebe, R. E., & Wolf-Gladrow, D. A. (2001). *CO_2 in Seawater: Equilibrium, Kinetics, Isotopes*. Elsevier.

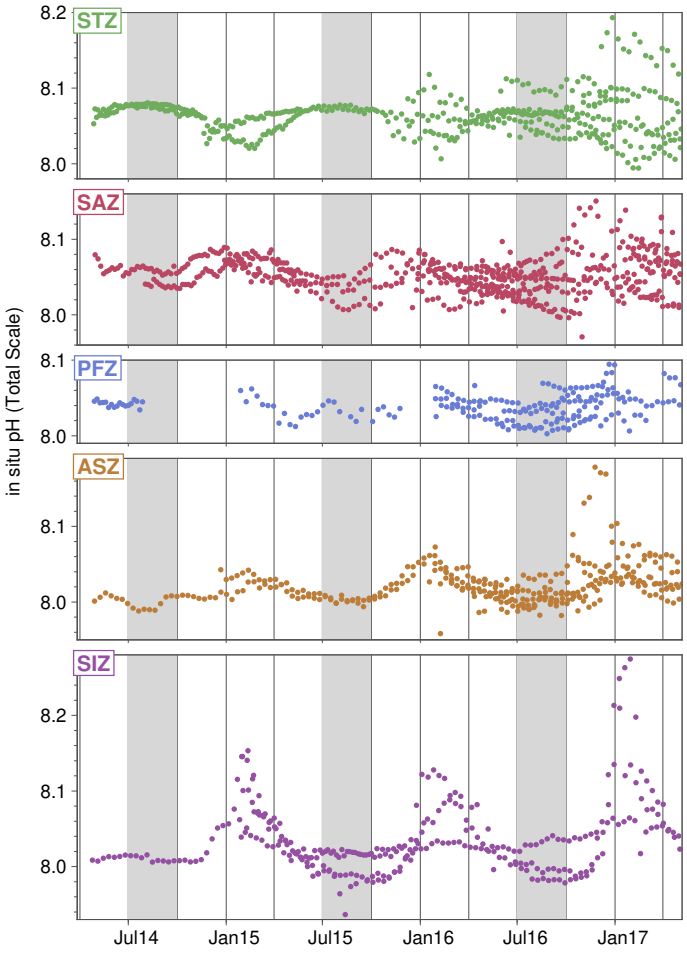

Figure S1. Measurements of pH for all floats in each zone. Light gray vertical bar highlights winter months (JAS).

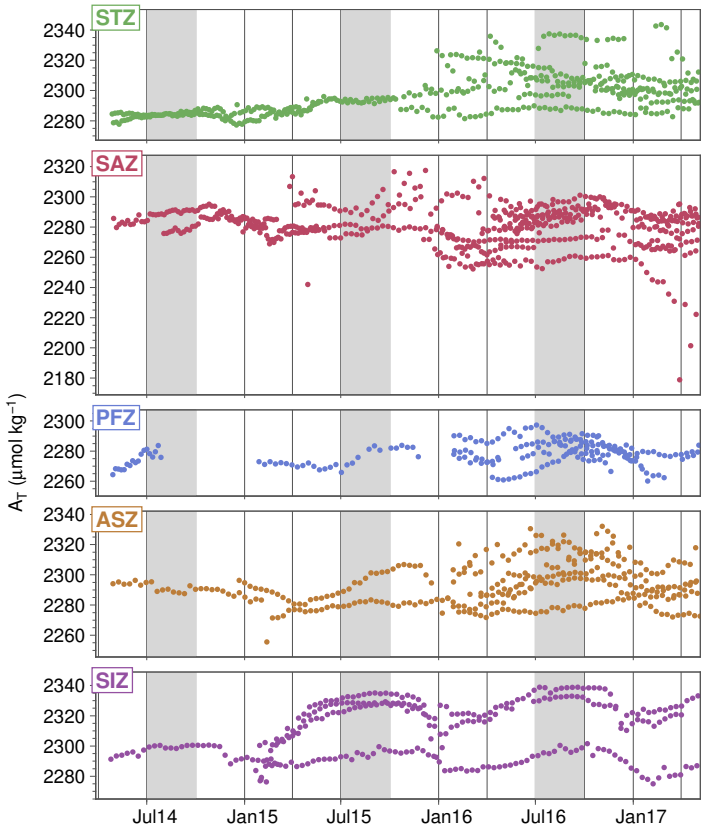

Figure S2. Estimates of A_T for all floats in each zone. Light gray vertical bar highlights winter months (JAS).

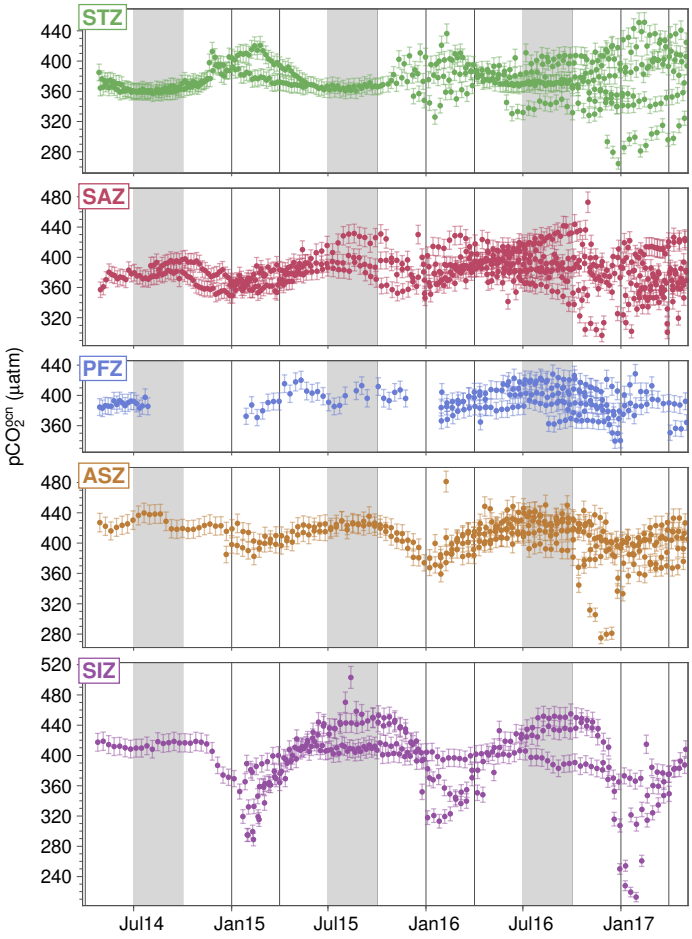

Figure S3. Estimates of pCO_2^{ocn} for all floats in each zone. Light gray vertical bar highlights winter months (JAS).

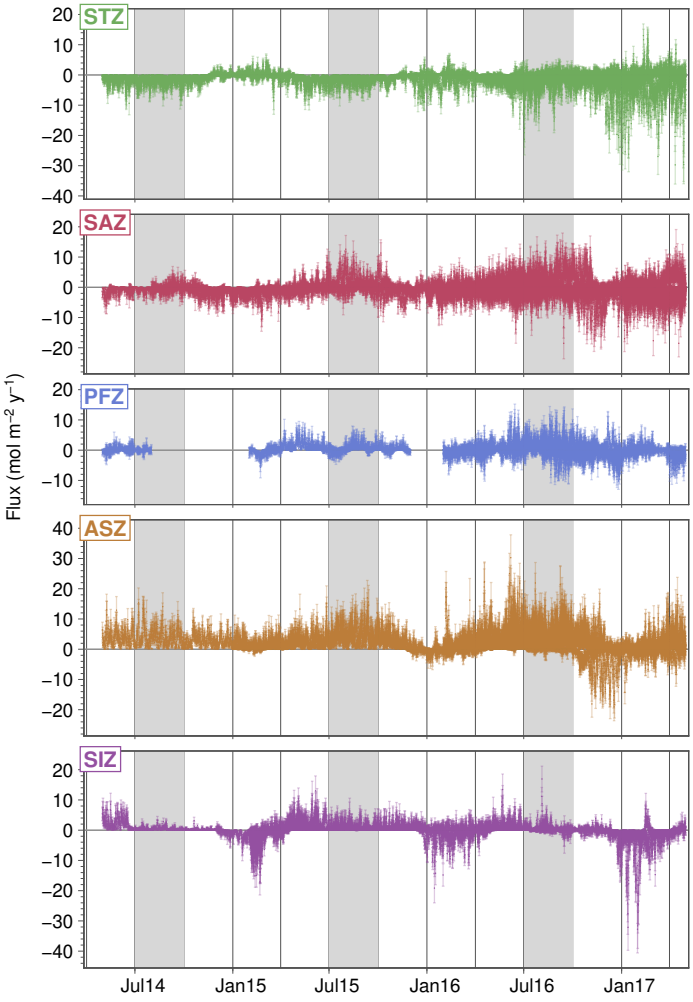

Figure S4. Estimates of air-sea CO_2 flux for all floats in each zone. Positive (negative) indicates flux out of (into) the ocean. Light gray vertical bar highlights winter months (JAS).

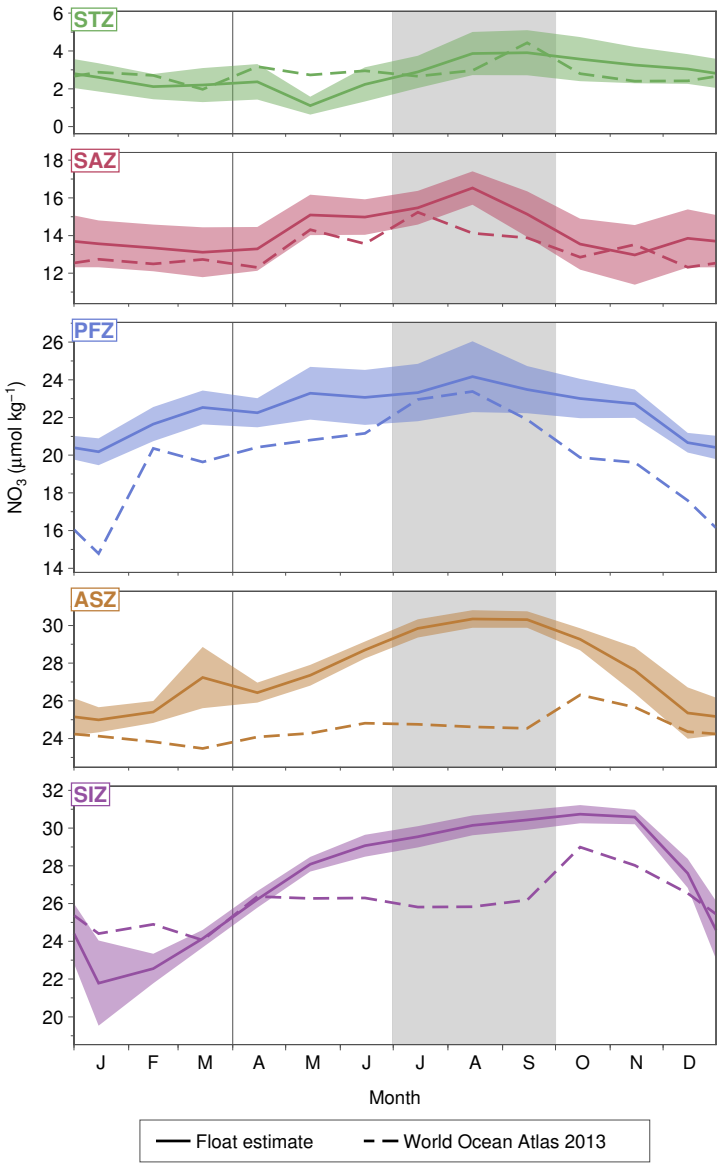

Figure S5. Monthly mean nitrate concentration in upper 20 m (or mixed layer if shallower than 20 m) from float measurements (colored line), averaged in the same way as the monthly flux estimates. The shading represents ±1 standard error for each monthly mean, estimated from the observed variance. Nitrate concentrations from the World Ocean Atlas 2013 seasonal climatology (Garcia et al., 2014) (dashed line) were calculated by sampling the climatological fields at the same locations as the float profiles and then constructing monthly means in each zone. Light gray vertical bar highlights winter months (JAS).

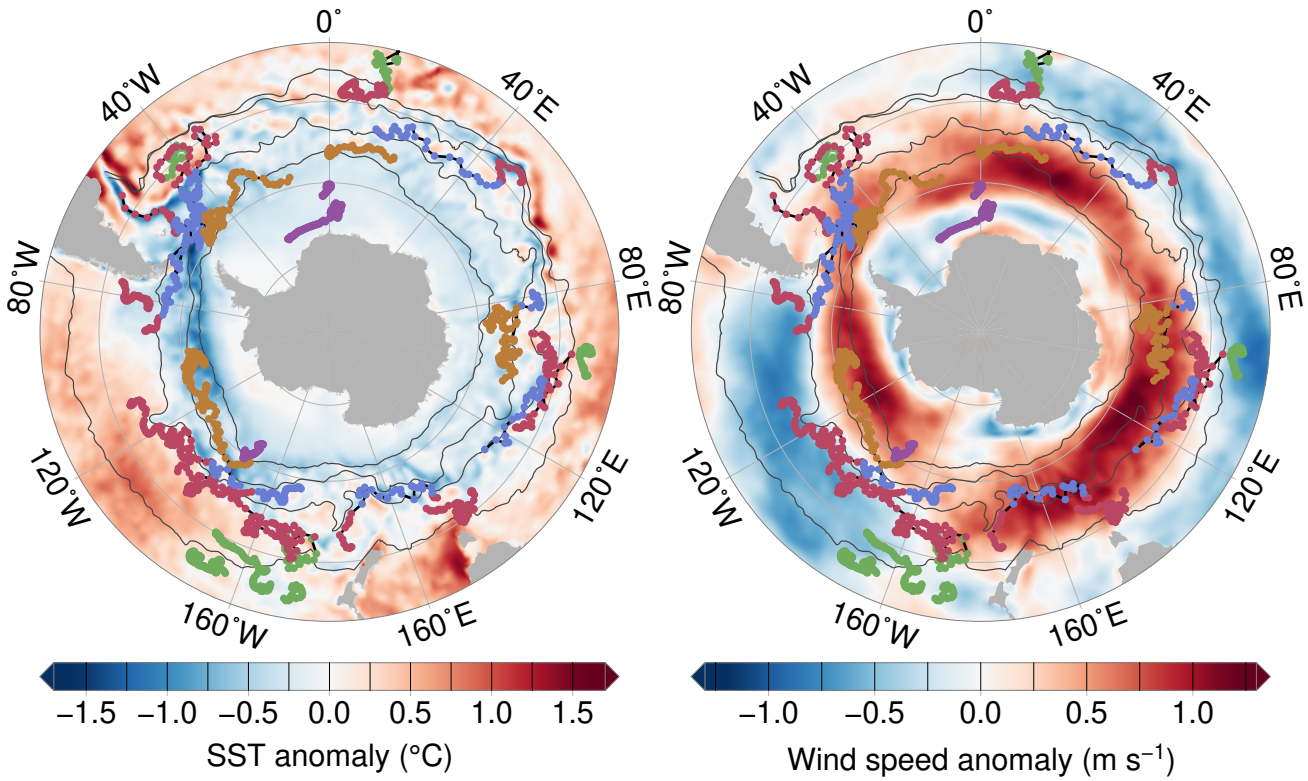

Figure S6. 2014-2016 anomalies for (a) sea surface temperature and (b) wind speed computed from ERA-Interim fields, relative to mean 1979-2016 fields. Float trajectories and zonal boundaries as in Figure 1.

Table S1. Identification number (WMO ID), deployment date and location, and number of months of data (Mon) in each zone, for each float used in this study. Each float is listed under all zones that it sampled; deployment location is only given for the zone initially sampled by the float. Total months of float data in each zone is given in parentheses.

Zone	WMO ID	Date	Location	Mon
	5904187	18 Apr 2014	44° 58.4'S, 149° 59.6'W	36
	5904395	20 Apr 2014	39° 39.4'S, 149° 59.0'W	36
	5904474	07 Dec 2014		16
STZ	5904675	07 Jan 2016	39° 27.1'S, 99° 28.2'E	15
(129)	5904657	09 Jan 2016		5
	5904693	20 May 2016	47° 59.8'S, 169° 58.4'W	8
	5904765	31 May 2016		6
	5904674	31 May 2016	39° 57.8'S, 172° 34.1'W	7
	5904396	11 Apr 2014		27
	5904186	13 Apr 2014	52° 29.3'S, 150° 0.6'W	10
	5904474	07 Dec 2014	44° 39.5'S, 7° 5.6'E	11
	5904473	27 Jan 2015		5
	5904187	27 Mar 2015	47° 8.6'S, 144° 0.6'E	15
	5904663	08 Dec 2015	53° 19.9'S, 80° 17.9'W	16
	5904661	28 Dec 2015	54° 15.7'S, 89° 15.1'W	9
	5904658	08 Jan 2016		3
SAZ	5904657	09 Jan 2016		7
(163)	5904682	01 Mar 2016	50° 35.8'S, 90° 23.9'E	13
	5904683	03 Mar 2016	47° 5.3'S, 93° 4.7'E	5
	5904688	06 Mar 2016	52° 45.5'S, 151° 4.1'E	2
	5904677	31 Mar 2016	50° 28.6'S, 147° 10.4'E	5
	5904678	07 Apr 2016	51° 57.1'S, 148° 40.0'E	3
	5904695	14 May 2016		2
	5904761	18 May 2016	51° 55.5'S, 169° 54.7'W	11
	5904763	19 May 2016	49° 57.8'S, 169° 47.0'W	11
	5904693	20 May 2016		3
	5904765	31 May 2016	46° 40.0'S, 171° 31.7'W	5

Zone	WMO ID	Date	Location	Mon
	5904396	11 Apr 2014	55° 0.3'S, 150° 1.0'W	3
	5904473	27 Jan 2015	49° 0.1'S, 12° 56.1'E	10
	5904662	28 Dec 2015	54° 15.7'S, 89° 15.2'W	8
	5904661	28 Dec 2015		7
PFZ	5904658	08 Jan 2016	57° 59.6'S, 56° 30.3'W	12
(70)	5904657	09 Jan 2016	56° 28.8'S, 57° 12.3'W	3
	5904679	18 Jan 2016	49° 45.9'S, 78° 49.4'E	3
	5904683	03 Mar 2016		8
	5904677	31 Mar 2016		7
	5904695	14 May 2016	57° 58.5'S, 169° 56.9'W	9
	5904185	07 Apr 2014	59° 59.5'S, 150° 1.2'W	36
	5904469	10 Dec 2014	53° 31.0'S, 0° 0.2'E	23
ASZ	5904660	07 Jan 2016	60° 37.6'S, 54° 38.1'W	15
(115)	5904659	07 Jan 2016	59° 38.2'S, 55° 23.0'W	15
	5904679	18 Jan 2016		12
	5904684	28 Feb 2016	52° 58.7'S, 87° 39.5'E	14
	5904184	03 Apr 2014	63° 59.6'S, 150° 1.4'W	36
SIZ	5904471	21 Dec 2014	64° 56.5'S, 4° 7.6'E	1
(102)	5904472	18 Jan 2015	67° 40.0'S, 1° 45.2'W	27
	5904468	19 Jan 2015	66° 1.5'S, 0° 2.0'E	27
	5904397	21 Jan 2015	61° 0.2'S, 0° 0.1'W	11

Table S2. Area and mean air-sea CO_2 flux in each Southern Ocean zone for float-based estimates and two ship-based estimates, *Tak09* (Takahashi et al., 2009) and *GCB17*, (Le Quéré et al., 2018). Positive (negative) flux indicates outgassing (uptake). Float-based estimates reported as mean and ±1 standard error, determined with Monte Carlo simulation (see Text S4). Flux from ship-based estimates given as the uptake in each region when those estimates were sampled at the position of the floats; numbers in parentheses give flux for all grid boxes in each region.

		Float-based flux		Ship-based flux	
Zone	Area [10^7 km^2]	Area-average [mol m^{-2} y^{-1}]	Total [PgC y^{-1}]	*Tak09* [PgC y^{-1}]	*GCB17* [PgC y^{-1}]
Subtropical (STZ)	2.26	-1.30 ± 0.44	-0.35 ± 0.12	-0.42 (-0.40)	-0.52 (-0.56)
Subantarctic (SAZ)	1.94	-0.43 ± 0.62	-0.10 ± 0.14	-0.30 (-0.23)	-0.26 (-0.27)
Polar Frontal (PFZ)	1.43	0.03 ± 0.67	0.01 ± 0.12	-0.14 (-0.16)	-0.05 (-0.11)
Antarctic-Southern (ASZ)	1.28	2.32 ± 0.74	0.36 ± 0.11	0.02 (0.00)	-0.03 (-0.03)
Seasonal Ice (SIZ)	1.72	0.04 ± 0.31	0.01 ± 0.06	0.02 (0.02)	-0.06 (-0.08)
Southern Ocean South of 35°S	8.64	LB uncertainty UB uncertainty	-0.08 ± 0.04 -0.08 ± 0.55	-0.81 (-0.77)	-0.94 (-1.05)